Smart Materials and Structures

Embedded piezoelectric ceramic transducers in sandwiched beams

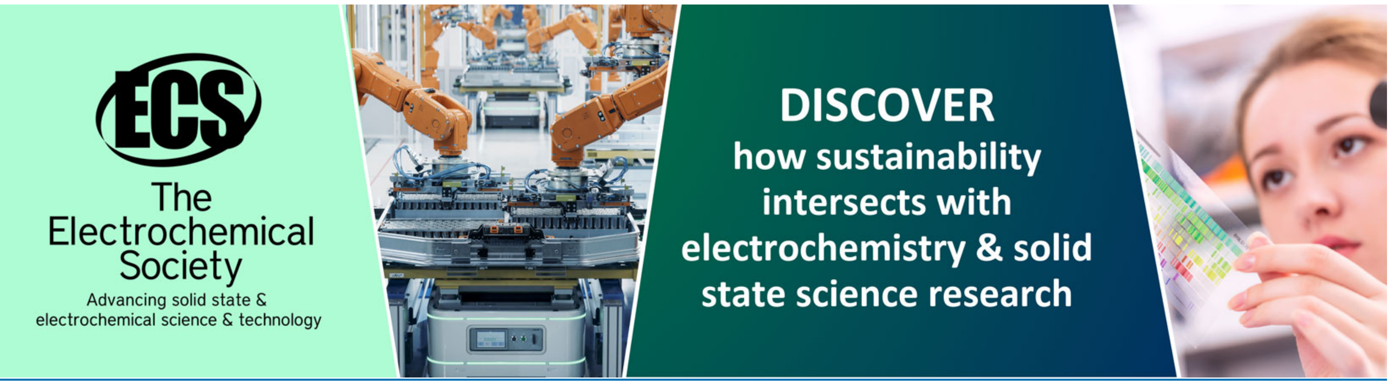

INSTITUTE OF PHYSICS PUBLISHING SMART MATERIALS AND STRUCTURES
Smart Mater. Struct. **15** (2006) 538–549 doi:10.1088/0964-1726/15/2/037

Embedded piezoelectric ceramic transducers in sandwiched beams

Venu Gopal Madhav Annamdas and Chee Kiong Soh[1]

School of Civil and Environmental Engineering, Nanyang Technological University, 50 Nanyang Avenue, 639798, Singapore

E-mail: vgmadhav@pmail.ntu.edu.sg and csohck@ntu.edu.sg

Received 23 February 2005, in final form 17 January 2006
Published 23 February 2006
Online at stacks.iop.org/SMS/15/538

Abstract
Surface bonded piezoelectric ceramic (PZT) transducers are currently the most prominent area of research in structural health monitoring using electromechanical impedance methods. This paper presents a new embedded PZT patch and its interaction with the host sandwiched beam. Durability and protection from surface finish, vandalism and the environment are important features of the embedment. The paper also demonstrates the use of thickness vibration of the PZT patch in electromechanical admittance formulations. This embedded PZT–structure interaction model is based on the new concept of 'average sum impedance'. The formulations used for this model can be conveniently employed to extract the mechanical impedance of any 'unknown' PZT patch embeddable plane structure. The mechanical impedance of the structure is obtained from the admittance signatures of the embedded PZT patch. The proposed model is experimentally verified on sandwiched beams.

(Some figures in this article are in colour only in the electronic version)

1. Introduction

1.1. The electromechanical impedance (EMI) method

Piezoelectric ceramic (PZT) material has emerged as a popular self-sensing material which can excite structures at high frequencies of the order of kilohertz. These patches, when activated at higher modes, facilitate the easy capture of minor structural damage (Doebling *et al* 1998). The application of PZT patches in the electromechanical impedance (EMI) method is one of the more recent developments in structural health monitoring (SHM). In this method, a PZT patch is either surface bonded to or embedded inside the host structure which is actuated in the presence of an electric field. The self-sensing PZT transducer enables the transduction of electric energy to mechanical energy, and vice versa, between the PZT patch and the host structure (Liang *et al* 1994, Bhalla and Soh 2004a). The electrical admittance (inverse of electrical impedance) of the bonded or embedded PZT patch is expressed as a coupling of the mechanical impedance of the actuator and the mechanical impedance of the host structure. Since the mechanical impedance of any structure is dependent on its material properties, structural configuration and boundary conditions, any damage will alter these properties and the alterations are induced in the mechanical impedance of the structure. These alterations are finally reflected in the electrical admittance of the PZT transducer. At any excited frequency, the PZT patch produces an admittance response known as the 'admittance signature'. The changes in these signatures are indicative of the presence of structural damage. This method was first used by Sun *et al* (1995), and was later successfully explored by many other researchers in the field of structural health monitoring (Ayres *et al* 1998, Giurgiutiu *et al* 1999, Park *et al* 2000, Soh *et al* 2000, Park *et al* 2001, 2003, Naidu and Soh 2004, Bhalla and Soh 2004a, 2004b, Peairs *et al* 2004).

The main assumption made by researchers of the EMI method is that the PZT patch is a bar undergoing uni-extensional actuation (axial vibrations) in the length direction (Liang *et al* 1994) or bi-extensional actuation in the length and the width directions (Bhalla and Soh 2004a). Generally, actuations of the PZT transducers in the presence of electric fields can be divided into extensional (along the X and Y directions), longitudinal (along the Z direction) and shear actuations (in the XZ and YZ planes), as shown in figure 1.

[1] Author to whom any correspondence should be addressed.

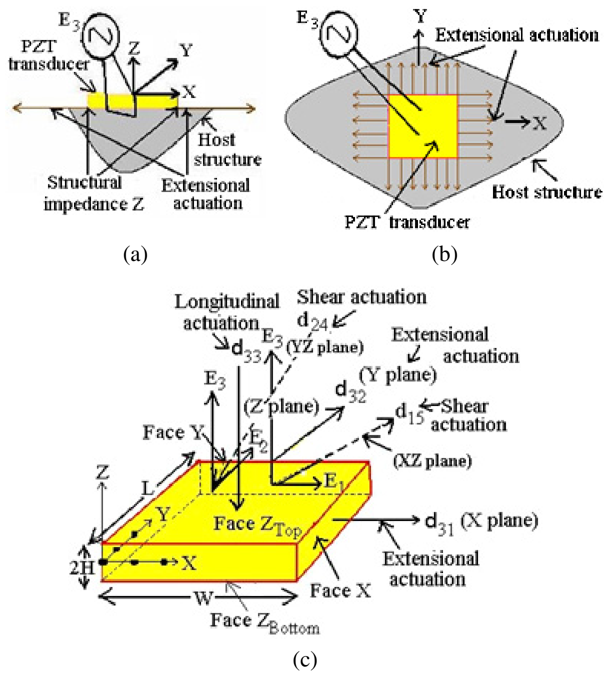

Figure 1. Actuation of a PZT transducer in the presence of electric fields E_1, E_2 and E_3: (a) one-dimensional interaction model, (b) two-dimensional interaction model and (c) three-dimensional interaction model.

Actuations of the PZT transducer along the X and Y directions are opposite in nature in comparison with actuation along the Z direction (Raja *et al* 2004). However, in the EMI method, the electric field is only applied along the Z direction; so actuations in the XZ and YZ planes do not exist but actuations along the X, Y and Z directions do exist. Many other researchers like Zhou *et al* (1996), Giurgiutiu *et al* (1999), Park *et al* (2003) and Peairs *et al* (2004) have also developed interaction models based only on extensional actuation (using length or width or both) of the PZT patch.

The major limitation of the existing models is that they ignore vibration of the PZT patch in the thickness direction. Moreover, the existing (EMI) models are not applicable to laminated or civil engineering structures where the sensitive zone to be monitored is inside the structure. The thickness vibration plays a vital role in thick or confined (embedded) PZT patches, and hence affects the structural response. The structural response depends on factors like PZT patch thickness, width, orientation, etc (Wetherhold *et al* 2003). Moreover, thickness vibration of the PZT patch is used in innumerable vibration and noise control applications (Raja *et al* 2004) but not in SHM. In general, the inability of the existing models to consider the thickness vibration and its inapplicability to embeddable structures had left a gap for the development of a new model.

This paper presents an embedded piezoimpedance patch and its interaction with the host sandwiched aluminium beam using extensional actuation (along the X direction) and longitudinal actuation (along the Z direction). Durability and protection from surface finishes, vandalism and the environment are important features of the embedment of the PZT patches. Thus where ever possible, it is sensible to use embedded an piezoimpedance patch and the interaction model instead of the existing surface bonded PZT interaction models. This embedded PZT–structure interaction model is based on the new concept of 'average sum impedance'. The formulations used for this model can be conveniently employed to extract admittance signatures of any 'unknown' plane structure into which a PZT patch can be embedded, especially in civil engineering structures, sandwiched beams, etc. During the period of SHM, any change in the admittance signature signifies damage in the structure, and thus this model can be conveniently applied for SHM of PZT embeddable plane structures. The proposed model is experimentally verified on a system comprising a PZT patch embedded inside the epoxy layer of a sandwiched aluminium beam (figure 2).

2. Average sum impedance model

In this paper, an analytical model of a PZT patch embedded in a sandwiched beam is presented, based on the 'average sum impedance (ASI) concept'. This is a generic two-dimensional (2D) (length and thickness) PZT patch–structure interaction model. The theoretical formulations are validated experimentally. For this purpose, a sandwiched beam was fabricated using two aluminium beams bonded by an epoxy layer with a PZT patch embedded inside the epoxy layer (figure 2). This analytical model effectively demonstrates the contribution of vibration in the thickness direction to the admittance formulations.

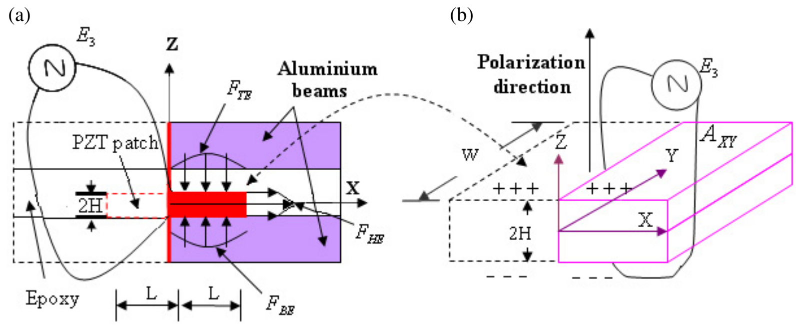

Figure 2. Electromechanical modelling of embedded PZT patches. (a) A PZT patch embedded in sandwiched aluminium beams. (b) Electric polarization of the embedded PZT patch.

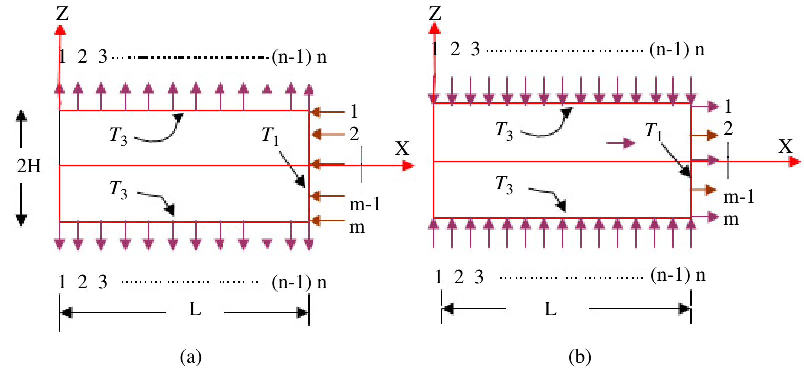

Figure 3. Behaviour of a PZT patch at any instant of time. (a) Expansion of the patch in direction X and shrinkage in direction Z. (b) Expansion of the patch in direction Z and shrinkage in direction X.

2.1. Fundamental PZT constitutive equations

Figure 2(a) shows a PZT patch embedded inside a sandwiched beam. Figure 2(b) shows the X, Y and Z directions along the length ($2L$), width (W) and thickness ($2H$), respectively, of the embedded PZT patch.

The derivations covered in this section are based on the following assumptions:

(1) The PZT patch material is mechanically isotropic.
(2) Plane strain conditions exist within the PZT patch; hence, only the X and Z directions are considered. For structures where plane strain conditions are not applicable, actuations along the X, Y and Z directions are to be considered.
(3) Force transmission between the embedded PZT patch and the host structure is distributed along both the X and Z directions, covering the entire contact area (figure 3).
(4) The PZT patch is infinitesimally small with negligible mass and stiffness compared with the host structure. However, if multiple PZT patches are used there could be a significant increase in the overall mass of the PZT patches; hence the mass has to be considered in the formulation.

Under a one-dimensional (1D) harmonic electric field (E_3) along direction Z, with an angular frequency ω, the interaction of one-half of the patch with one-half of the host sandwiched structure is considered, taking advantage of symmetry about direction Z as shown in figure 2(a).

Considering directions X and Z, the general 2D stress and strain relationship can be written as

$$\begin{Bmatrix} T_1 \\ T_3 \end{Bmatrix} = \bar{Y}^{\mathrm{E}} \frac{(1-\nu)}{(1+\nu)(1-2\nu)} \times \begin{bmatrix} 1 & \nu/(1-\nu) \\ \nu/(1-\nu) & 1 \end{bmatrix} \begin{bmatrix} S_1 \\ S_3 \end{bmatrix} \tag{1}$$

where T_1 and T_3 are the stresses applied on the PZT patch in directions X and Z, respectively, and ν is the Poisson ratio. $\bar{Y}^{\mathrm{E}}$ is the complex Young's modulus of elasticity of the PZT patch at zero electric field, and it can be expressed as

$$\bar{Y}^{\mathrm{E}} = Y^{\mathrm{E}}(1+\eta \mathrm{j}) \tag{2}$$

where Y^{E} is the static Young's modulus of elasticity of the PZT material and η is the mechanical loss factor.

Equation (1) can be rearranged to produce the strain equations, S_1 and S_3, in directions X and Z, respectively, as

$$S_1 = \frac{aT_1 + bT_3}{\bar{Y}^{\mathrm{E}}} \tag{3a}$$

$$S_3 = \frac{bT_1 + aT_3}{\bar{Y}^{\mathrm{E}}} \tag{3b}$$

where a and b are two constants such that

$$a = \frac{(1+\nu)(1-2\nu)^2}{(1-\nu)^3} \quad \text{and} \quad b = \nu \frac{(1+\nu)(2\nu-1)}{(1-\nu)^4}. \tag{4}$$

Thus, the fundamental relationships of the PZT patch in the presence of an electric field can be written as

$$S_1 = \frac{aT_1 + bT_3}{\bar{Y}^{\mathrm{E}}} + d_{31}E_3 \tag{5a}$$

$$S_3 = \frac{bT_1 + aT_3}{\bar{Y}^{\mathrm{E}}} + d_{33}E_3. \tag{5b}$$

The electric displacement (or charge density), D_3, (where the subscript 3 denotes the electric field in the direction Z) over the surface of the PZT patch can be written as

$$D_3 = \varepsilon_{33}^{\bar{T}} E_3 + d_{31}T_1 + d_{33}T_3 \tag{5c}$$

where d_{Zj} represents the piezoelectric strain coefficient of the PZT, subscript Z signifies the direction of the electric field and j signifies the direction of the resulting stress (or strain). $\varepsilon_{33}^{\bar{T}}$ is the complex electric permittivity of the PZT at zero stress, and can be expressed as

$$\varepsilon_{33}^{\bar{T}} = \varepsilon_{33}^{T}(1-\delta \mathrm{j}) \tag{6}$$

where δ is the dielectric loss factor and ε_{33}^{T} is the static electric permittivity of the PZT patch.

2.2. ASI of the actuator

Figure 2 shows a PZT patch embedded in the epoxy layer (RS 850-940 epoxy adhesive, RS Components 2004) of the sandwiched specimen.

Table 1. Key properties of PZT grade PIC 151 (PI Ceramic 2004).

	Physical property	Value
1	Density (kg m^{-3})	7800
2	Young's modulus (N m^{-2})	6.667×10^{10}
3	Poisson ratio	0.33
4	Electric permittivity, ε_{33} (F m^{-1})	2.124×10^{-8}
5	Piezoelectric strain coefficient in direction X, d_{31} (m V^{-1})	-2.10×10^{-10}
6	Piezoelectric strain coefficient in direction Z, d_{33} (m V^{-1})	4.50×10^{-10}
7	Dielectric loss factor, δ	0.015
8	Mechanical loss factors η	0.023

At any instant of time, the forces developed due to the actuation of the PZT patch as shown in figure 3, which respectively correspond to expansion in direction X and shrinkage in direction Z, or vice versa. The forces take into consideration the alternate signs of d_{31} and d_{33}, as listed in table 1. Due to the alternate signs, the expansion of the patch in direction X is accompanied by shrinkage in direction Z, and vice versa. The ASI of the actuator can be represented mathematically as

$$Z_{\mathrm{as}} = \frac{\mathrm{FP_H}}{\frac{1}{m}\sum_1^m \dot{u}_{m1}} + \frac{2\mathrm{FP_T}}{\frac{1}{n}\sum_1^n \dot{u}_{n3}} = \frac{\mathrm{FP_H}}{\dot{u}_{1(X=L)}} + \frac{2\mathrm{FP_T}}{\dot{u}_{3(Z=H)}} \quad (7)$$

where Z_{as} is the average sum of the actuator impedance, $\mathrm{FP_H}$ and $\mathrm{FP_T}$ are the total force components acting on the PZT patch along directions X and Z, respectively, m and n are the finite number of points considered along the boundary (at $X = L$ and $Z = \pm H$, respectively), $\dot{u}_{m3}$ is the velocity of the mth point in direction Z, $\dot{u}_{n1}$ is the velocity of the nth point in direction X, $\dot{u}_{1(X=L)}$ is the average velocity in direction X at $X = +L$ and $\dot{u}_{3(Z=H)}$ is the average velocity in direction Z at $Z = \pm H$ of the PZT patch.

As described in equation (7), the average velocities in directions X and Z are determined first, and the ratios of the force components to the average velocities are then calculated. Finally, these ratios are added to obtain the average sum actuator impedance, hence this is called the 'average sum impedance' (ASI) model. The final value of the actuator impedance is the same irrespective of the direction considered, as shown in figure 3.

2.3. Derivation of the actuator impedance from stress–strain relationships of the PZT

Using strain equations (3*a*) and (3*b*), in short-circuited condition, i.e. $E_3 = 0$, the equations for the stresses acting on the PZT patch can be written as

$$T_1 = \bar{Y}^{\mathrm{E}} \frac{S_1 a - S_3 b}{a^2 - b^2} \quad (8a)$$

$$T_3 = \bar{Y}^{\mathrm{E}} \frac{S_3 a - S_1 b}{a^2 - b^2}. \quad (8b)$$

Let u_1 be the average displacement developed along direction X and u_3 be the average displacement developed along direction Z. The displacement equations for two directional in-plane vibrations are derived similar to that of Zhou *et al* (1996), which can be expressed as

$$u_1 = (A \sin kx)\mathrm{e}^{\mathrm{j}\omega t} \quad (9a)$$

$$u_3 = (C \sin kz)\mathrm{e}^{\mathrm{j}\omega t} \quad (9b)$$

where A and C are the coefficients of vibration, which are to be determined from the boundary conditions, and k is the wavenumber given by

$$k = \omega \sqrt{\frac{\rho(1+\nu)(1-2\nu)}{\bar{Y}^{\mathrm{E}}(1-\nu)}} \quad (10)$$

where ω is the angular frequency of vibration, related to natural frequency f as

$$\omega = 2\pi f \quad (11)$$

and ρ is the density of the PZT patch material. For simplicity, let

$$C = \alpha_P A \quad (12)$$

where α_P is a factor dependent on the material properties and dimensions of the PZT. The interaction between the embedded PZT patch and the host structure is not completely characterized by the basic material properties such as Young's modulus, piezoelectric constant, dielectric constant and electromechanical coupling factor (Wang and Shen 1998). Hence the factor α_P is introduced into this model to simplify the formulations. The detailed procedure for determining its value is covered in section 3.2.

Differentiating equations (9*a*) and (9*b*) with respect to time, and using equation (12), the velocities in the X and Z directions can be written as

$$\dot{u}_1 = \mathrm{j}\omega A(\sin kx)\mathrm{e}^{\mathrm{j}\omega t} \quad (13a)$$

$$\dot{u}_3 = \alpha_P \mathrm{j}\omega A(\sin kz)\mathrm{e}^{\mathrm{j}\omega t}. \quad (13b)$$

Further, differentiating equations (9*a*) and (9*b*) with respect to x and z, the strains in the X and Z directions can be written as

$$S_1 = \frac{\partial u_1}{\partial x} = Ak(\cos kx)\mathrm{e}^{\mathrm{j}\omega t} \quad (14a)$$

$$S_3 = \frac{\partial u_3}{\partial z} = \alpha_P Ak(\cos kz)\mathrm{e}^{\mathrm{j}\omega t}. \quad (14b)$$

Also, equation (7) can be written as

$$Z_{\mathrm{as}} = \frac{T_1 W(2H)}{\dot{u}_{1(X=L)}} + \frac{2T_3 WL}{\dot{u}_{3(Z=H)}} \quad (15)$$

where the forces are replaced by the stresses acting on the boundary multiplied by the areas on which the stresses act. Substituting equations (8*a*), (8*b*) and (13) into equation (15), the following expression is derived for Z_{as}:

$$Z_{\mathrm{as}} = \frac{W\bar{Y}^{\mathrm{E}}k}{\mathrm{j}\omega(a^2-b^2)}\left[\frac{H(2a\cos kL - b\alpha_P\cos kH)}{\sin kL} + \frac{L(a\alpha_P\cos kH - 2b\cos kL)}{\alpha_P \sin kH}\right]. \quad (16)$$

Further, let N be a substitute variable, as given below

$$N = \left[\frac{H(2a\cos kL - b\alpha_P\cos kH)}{\sin kL} + \frac{L(a\alpha_P\cos kH - 2b\cos kL)}{\alpha_P \sin kH}\right]. \quad (17)$$

With this substitution, the mechanical impedance of the actuator (equation (16)) can be written in a closed form as

$$Z_{\mathrm{as}} = \frac{W\bar{Y}^{\mathrm{E}}kN}{\mathrm{j}\omega(a^2-b^2)}. \tag{18}$$

2.4. ASI of the host structure

In this derivation, the ASI approach described in the previous section is again adopted. The mechanical impedance of the structure is determined in the presence of an electric field (i.e. $E_3 \neq 0$).

Figure 2 shows an embedded PZT patch in the presence of an electric field, E_3, where F_{TE}, F_{BE} and F_{HE} are the total forces acting on the respective faces due to actuation in the PZT patch caused by the presence of E_3.

The size of the PZT patch is very small compared with the host structure. Hence a uniform stress distribution prevails along the top and bottom edges of the PZT patch, and they are assumed to act on equal areas (eventually leading to $F_{\mathrm{TE}} = F_{\mathrm{BE}} = F$). Thus, the structural impedance can be written as

$$-Z_{\mathrm{s}} = \frac{F_{\mathrm{HE}}}{\dot{u}_{1(X=L)}} + \frac{2F}{\dot{u}_{3(Z=H)}}. \tag{19}$$

The negative sign indicates that a positive average displacement in the X or Z direction causes compression in the patch (due to reaction from the structure).

The electric field is given by

$$E_3 = \frac{V_0}{2H}\mathrm{e}^{\mathrm{j}\omega t} \tag{20}$$

where V_0 is the instantaneous voltage across the PZT patch.

Using equations (5*a*)–(5*c*), the stresses acting along the X and Z directions can be written as

$$T_1 = \frac{(S_1a - S_3b)\bar{Y}^{\mathrm{E}}}{a^2-b^2} + \frac{\bar{Y}^{\mathrm{E}}E_3}{a^2-b^2}(d_{33}b - d_{31}a) \tag{21a}$$

$$T_3 = \frac{(S_3a - S_1b)\bar{Y}^{\mathrm{E}}}{a^2-b^2} + \frac{\bar{Y}^{\mathrm{E}}E_3}{a^2-b^2}(d_{31}b - d_{33}a). \tag{21b}$$

Substituting equations (16), (21*a*) and (21*b*) into (19), the ASI of the structure can be written as

$$Z_{\mathrm{s}} + Z_{\mathrm{as}} = (-1)\frac{\bar{Y}^{\mathrm{E}}V_0W}{A(2H)(a^2-b^2)\mathrm{j}\omega} \times \left[\frac{2H(d_{33}b - d_{31}a)}{\sin kL} + \frac{2L(d_{31}b - d_{33}a)}{\alpha_P \sin kH}\right]. \tag{22}$$

Substituting

$$A_0 = A\Big/\left(\frac{V_0}{H}\right) \tag{23}$$

into equation (22) and after rearranging, the following expression is obtained:

$$A_0 = \frac{\bar{Y}^{\mathrm{E}}W}{2(a^2-b^2)\mathrm{j}\omega(Z_{\mathrm{as}} + Z_{\mathrm{s}})} \times \left[\frac{2H(d_{31}a - d_{33}b)}{\sin kL} + \frac{2L(d_{33}a - d_{31}b)}{\alpha_P \sin kH}\right]. \tag{24}$$

In equation (24), Z_{as}, Z_{s} and A_0 exist together. Although Z_{as} can be determined from equation (18), there are no closed form solutions for Z_{s} and A_0. Therefore, Z_{s} has to be determined using the finite element method (FEM) described in detail in the following section. Then, using Z_{s}, the coefficient A_0 is calculated, and then coefficient A is calculated using equation (23).

2.5. Expression for complex electromechanical admittance

Substituting equations (21*a*) and (21*b*) into (5*c*), the electric displacement can be written as

$$D_3 = \bar{\varepsilon}_{33}^{T}\frac{V_0}{2H}\mathrm{e}^{\mathrm{j}\omega t} + \frac{d_{31}\bar{Y}^{\mathrm{E}}}{a^2-b^2} \times \left[(S_1a - S_3b) + \frac{V_0}{2H}\mathrm{e}^{\mathrm{j}\omega t}(d_{33}b - d_{31}a)\right] + \frac{d_{33}\bar{Y}^{\mathrm{E}}}{a^2-b^2}\left[(S_3a - S_1b) + \frac{V_0}{2H}\mathrm{e}^{\mathrm{j}\omega t}(d_{31}b - d_{33}a)\right]. \tag{25}$$

Electric current is the rate of change of total electric charge over the surface (either the top or bottom surface which share opposite charges), as shown in figure 2(b). Hence, the electric current I can be written as

$$I = \int\int_{A_{XY}} \dot{D}_3\,\mathrm{d}x\,\mathrm{d}y = W\int_{X=-L}^{X=L} \dot{D}_3\,\mathrm{d}x = 2\mathrm{j}\omega W\int_0^L D_3\,\mathrm{d}x \tag{26}$$

where A_{XY} is the total surface area. Here there is no variation along the Y direction (width W is constant) but there exists variation along the X direction.

Electrical admittance is the ratio of the electric current to the applied electrical voltage. The electric admittance $\bar{Y}_{\mathrm{at}}$ and the applied voltage V across the PZT patch are expressed as

$$\bar{Y}_{\mathrm{at}} = \frac{I}{V} \qquad \text{and} \qquad V = V_0\mathrm{e}^{\mathrm{j}\omega t}. \tag{27}$$

Hence, using equations (26) and (27), the final complex electromechanical admittance of the PZT patch is obtained as

$$\bar{Y}_{\mathrm{at}} = \frac{\mathrm{j}\omega W}{H}\bigg(L\bar{\varepsilon}_{33} + \frac{d_{31}\bar{Y}^{\mathrm{E}}}{a^2-b^2} \times \{(2a\sin kL - b\alpha_P kL\cos kH)A_0 + L(d_{33}b - d_{31}a)\} + \frac{d_{33}\bar{Y}^{\mathrm{E}}}{a^2-b^2}\{(\alpha_P akL\cos kH - 2b\sin kL)A_0 + L(d_{31}b - d_{33}a)\}\bigg). \tag{28}$$

The procedure for finding the unknowns α_P and A is described in later sections. Equation (28) is the complete expression for the admittance of the embedded PZT patch.

3. Experimental and numerical analysis

This section describes the experimental setup, initialization, determination of the ASI of the structure using a numerical method, experimental verification and convergence testing.

3.1. Experimental setup

Figure 4 shows the experimental setup used for both ‘experimental initialization’ and ‘experimental verification’. The setup used for acquiring the admittance signature consisted of a HP 4192A impedance analyser (Hewlett Packard 1996), a 3499A/B switching box (Agilent Technologies 2004) and a personal computer. In both the ‘experimental initialization’ and ‘experimental verification’, the PZT patch was wired to the impedance analyser through the switch box. The signature of the experimental mechanical admittance, which consists of the real part (conductance) and the imaginary part (susceptance),

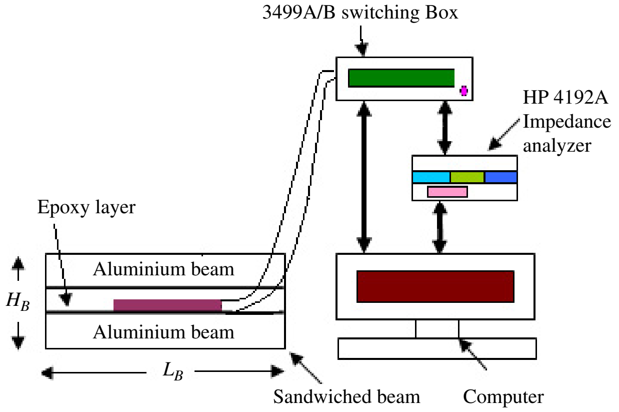

Figure 4. Experimental setup to verify the ASI-based impedance method.

Table 2. Key properties of epoxy adhesive (RS 850-940) and Al 6061-T6.

	Property	Epoxy adhesive	Aluminium (Al)
1	Density (kg m^{-3})	1180	2715
2	Young's modulus (N m^{-2})	2×10^9	68.95×10^9
3	Poisson ratio	0.4	0.33
4	Damping factor (β_M)	1.5923×10^{-9}	1.5923×10^{-7}

was acquired for the desired frequency range of <200 kHz for experimental initialization and <120 kHz for experimental verification. The highest frequency range to date used by any researcher (Naidu and Soh 2004) for beams is <60 kHz.

The sandwiched beam specimens used in the experimental verification were fabricated using aluminium beams of grade A1 6061-T6 (table 2), high-strength epoxy adhesive (RS Components 2004, table 2) and a PZT patch of grade PIC (PI Ceramic 2004, table 1). In order to prepare each specimen, a PZT patch was first surface bonded at the centre of the bottom aluminium beam using a very thin (negligible) epoxy adhesive. After allowing for initial setting, an epoxy layer of a certain thickness (as listed in table 3) was applied over the entire surface of the bottom aluminium beam and the bonded PZT patch. Another aluminium beam was placed over this epoxy layer (figure 2) and the whole arrangement was allowed to cure for 24 h with a nominal pressure applied over the entire arrangement throughout the curing time. The PZT patch, which is sandwiched between the two aluminium beams, thus behaved as an embedded patch in the epoxy layer. The embedded patch was connected to an impedance analyser which recorded the admittance signature (structure response). Details of the dimensions of the sandwiched beam specimens and embedded PZT patches are listed in table 3.

3.2. Experimental initialization

Before using the electromechanical admittance equation (28) for comparison with the experimental results, it is necessary to determine the ASI of the actuator (Z_{as}) and the host structure (Z_s). To find the impedance of the actuator and the host structure, α_P needs to be determined. The electromechanical admittance $\bar{Y}_{at}$ (equation (28)) is a complex term, and can be

Table 3. Details of specimens and PZT patch.

Specimen no.	Layers/ PZT patch	Length (m)	Width (m)	Height (m)
1	Al (top and bottom)	0.230	0.026	0.0020
	Epoxy (middle)	0.230	0.026	0.0010
	Total specimen dimensions ($2L_{Bm} \times W_{Bm} \times 2H_{Bm}$)	0.230	0.026	0.0050
	PZT ($2L \times W \times 2H$)	0.010	0.010	0.0002
2	Al (top and bottom)	0.140	0.026	0.0020
	Epoxy (middle)	0.140	0.026	0.0012
	Total specimen dimensions ($2L_{Bm} \times W_{Bm} \times 2H_{Bm}$)	0.140	0.026	0.0052
	PZT ($2L \times W \times 2H$)	0.010	0.010	0.0003

separated into real (conductance) and imaginary (susceptance) parts as given below.

$$\bar{Y}_{\rm at} = G + Bj. \tag{29}$$

The free (unembedded) signatures of two PZT patches were experimentally obtained before embedding the PZT patches into the specimens, using an impedance analyser and multiplexer (Bhalla and Soh 2004a). The unknown α_P was determined using experimental comparisons as described below.

Factor α_P is an unknown parameter; this is determined by matching the experimental conductance and susceptance signatures of the PZT patch in the 'free–free' condition with the analytical free conductance and susceptance signatures, respectively. From equations (24) and (28), to get the free analytical (PZT patch in free–free condition) admittance signature, a value of 'zero' is substituted for Z_s in equation (24), which resulted in

$$A_{0-\rm Free} = \frac{\bar{Y}^{\rm E} W}{2(a^2 - b^2){\rm j}\omega(Z_a)} \times \left[\frac{2H(d_{31}a - d_{33}b)}{\sin kL} + \frac{2L(d_{33}a - d_{31}b)}{\alpha_P \sin kH}\right] \tag{30}$$

where $A_{0-\rm Free}$ is the coefficient of vibration in the absence of Z_s.

Substituting equation (30) in (28), the complex admittance of the free PZT patch is obtained as

$$\begin{aligned}\bar{Y}_{Fr-at} = \frac{{\rm j}\omega W}{H}\bigg(L\bar{\varepsilon}^T_{33} + \frac{d_{31}\bar{Y}^{\rm E}}{a^2 - b^2}\{(2a \sin kL \\ - b\alpha_P kL \cos kH)A_{0-\rm Free} + L(d_{33}b - d_{31}a)\} \\ + \frac{d_{33}\bar{Y}^{\rm E}}{a^2 - b^2}\{(\alpha_P akL \cos kH - 2b \sin kL)A_{0-\rm Free} \\ + L(d_{31}b - d_{33}a)\}\bigg)\end{aligned} \tag{31}$$

where $\bar{Y}_{Fr-at}$ is the complex admittance of free PZT and can be split into the sum of conductance and susceptance as

$$\bar{Y}_{Fr-at} = G_{\rm Free} + {\rm j}B_{\rm Free}. \tag{32}$$

Thus, the derived admittance equation is independent of the host structure but depends on the PZT patch. Equation (31) is used to obtain the $G_{\rm Free}$ and $B_{\rm Free}$ signatures for the free PZT patch, which correspond to the different trial values of α_P. The particular value of α_P at which the analytical signature and

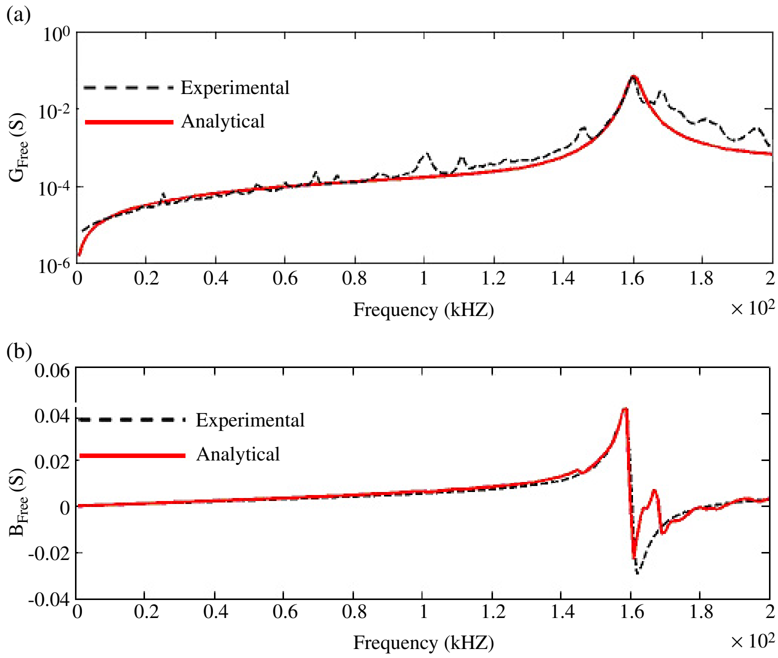

Figure 5. Plots of free PZT patch signatures of specimen 1. (a) Conductance signatures (experimental versus analytical). (b) Susceptance signatures (experimental versus analytical).

experimental signature match satisfactorily is adopted for that PZT patch. The values of α_P obtained for the PZT patches embedded inside the two sandwiched specimens obtained by trial and error are 0.02 and 0.12, respectively.

However, to obtain the trial and error value of α_P for the PZT patch, it is advisable to begin the initial guess for α_P with a 'reasonable' value. This 'reasonable' value can be obtained using the constant axial strain assumption as explained below.

For a mechanically isotropic bar, the elongation (or compression) is proportional to the overall dimension (length/width) of the bar. In the absence of an electric field, just for the initial 'reasonable' guess, free PZT patch behaviour is assumed to be similar to that of a mechanically isotropic bar. Mathematically, taking the ratio of amplitudes of displacements of equations (9*a*) and (9*b*), and using (12), the following equation is obtained:

$$\left|\frac{u_1}{u_3}\right| = \frac{A}{\alpha_P A} = \frac{L}{H}. \tag{33}$$

For the free PZT patch, from figure 3, the points of consideration are on the boundary. Hence equation (33) can be written as

$$\alpha_P = \frac{H}{L} = D_F \tag{34a}$$

where H and L are the half-height and half-length, respectively, of the PZT patch and D_F is a dimensional factor.

After the initial 'reasonable' assumption, many trials were made to predict the final value of α_P. This was done by matching the analytically obtained conductance and susceptance signatures of the free PZT patch in the 'free–free' condition using the trial values of α_P with the experimental conductance and susceptance of the free PZT patch in the 'free–free' condition.

Table 4. Material properties and α_P variations for specimen 1.

Density (kg m^{-3})	7800	8005	8095
Dielectric loss factor, δ	0.015	0.012	0.013
Mechanical loss factors, η	0.023	0.025	0.0205
Electric permittivity, ε_{33} ($\times 10^{-8}$ F m^{-1})	2.125	2.225	2.325
α_P	D_{F1}	$1.8D_{F1}$	$2.0D_{F1}$

From experiments, it was found that changes in some of the material properties of the PZT patch changed the predicted value of α_P. Three different α_P values are listed in table 4 for the change in some of the material properties of specimen 1. Other material properties are found not to have changed the α_P values. Hence, α_P is written as

$$\alpha_P = (\mathrm{MP}_F)D_F \tag{34b}$$

where MP_F is a material property factor.

Figures 5 and 6 show plots of the analytical and experimental admittance signatures for the free PZT patches of the specimens. Satisfactory agreement of both experiment and analytical conductance and susceptance show that the values obtained for α_P for both the PZT patches are reliable and can be used in determining the mechanical impedance of the actuator and the structure. The additional peaks as shown in figure 6 of the experimental admittance signature are due to the deviation in the shape of the PZT patch from a perfect square during manufacturing. This leads to partly independent peaks corresponding to the two slightly unequal edge lengths. It is reported in the literature that the properties of piezoceramic patches vary due to inhomogeneous chemical composition and mechanical differences during the formation and polarization process (Sensor Technology Limited 1995), and statistical variations are reported to be common (Giurgiutiu and Zagrai 2000).

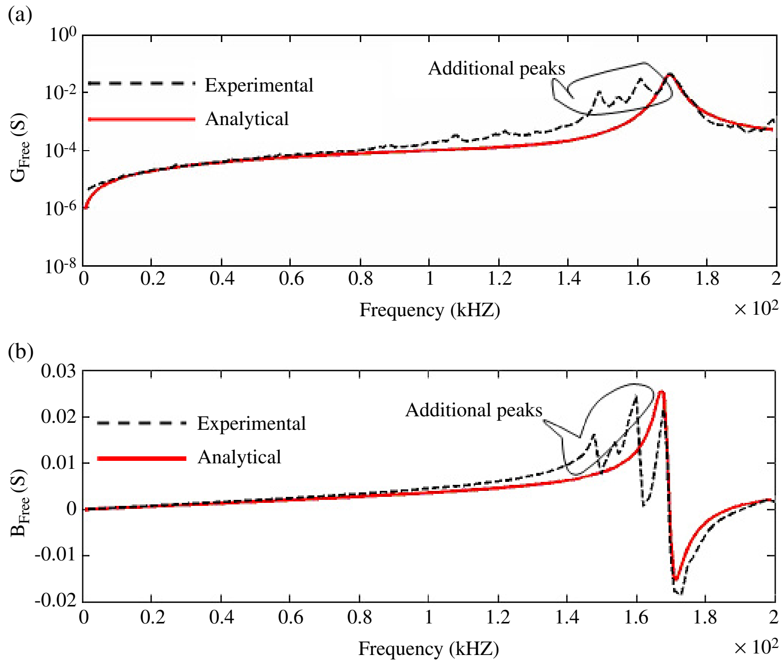

Figure 6. Plots of free PZT signatures of specimen 2. (a) Conductance signatures (experimental versus analytical). (b) Susceptance signatures (experimental versus analytical).

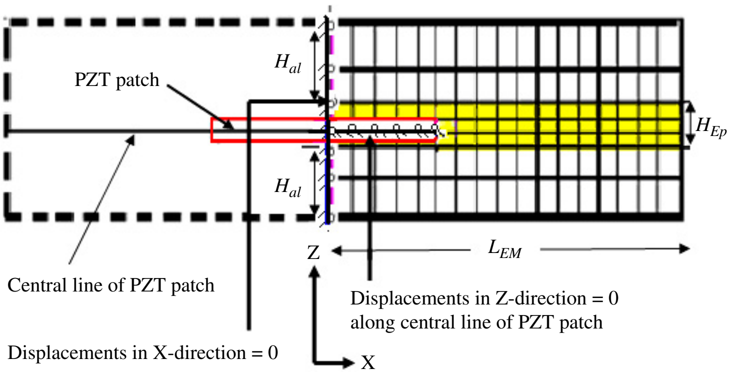

Figure 7. Finite element mesh of half of the specimen.

A frequency range of 0–200 kHz was considered, and a peak match of both experimental and analytical conductance and susceptance signatures was obtained at 160 and 170 kHz for specimens 1 and 2, respectively.

3.3. Determination of structural mechanical impedance using a FEM

Actuator impedance (Z_{as}), as described in the previous section, is determined by substituting the value of α_P into equation (17) and then solving equation (18). Unlike the actuator impedance Z_{as}, a simple closed-form solution is not available for the structural impedance Z_s. Hence, for complex systems one needs to rely on FEM as this is the most widely used tool in non-destructive evaluation methods. Therefore in this study, this tool was employed as it has the ability to model real-life complex structures.

Recently, researchers such as Makkonen *et al* (2001) demonstrated that in dynamic analysis problems excitation of very high frequencies (even up to the GHz range) can be modelled with good accuracy using FEM. Bhalla and Soh (2004a) (who excited frequencies of >200 kHz) used FEM to verify their impedance model. The excitation of test specimens with a harmonic electric field was compared with linear steady state forced vibration, and the new ASI 2D impedance model was verified as below.

The sandwich specimen was discretized into 2D quadrilateral elements as shown in figure 7. Since the structure was symmetric about the Z direction, only the right half of the structure was modelled. The experimental free–free condition was idealized by using appropriate boundary conditions, and the X component of displacement along the Z direction (i.e. the axis of symmetry) and the Z component of displacement up to the end of the patch along the X direction were set to zero.

As shown in figure 7, H_{al} is the thickness of the top and bottom aluminium layers, H_{Ep} is the thickness of the epoxy layer, and L_{BM} is the half-length of the beam specimen. The finite element (FE) analysis was carried out using ANSYS 5.6 (ANSYS 2000), with differential element mesh sizes (different sizes for different layers namely, aluminium top and bottom, and the epoxy layer). The element used is the 2D quadrilateral element (solid 42, four nodes), with two degrees of freedom at each node. Details of the mesh sizes and convergence criteria are discussed in the next section.

The PZT patch was not discretized since in the actuator impedance Z_{as} (admittance equations (18) and (28)), the stiffness and damping of the PZT patch were already included (Liang *et al* 1994, Bhalla and Soh 2004a). The following differential equation is employed (ANSYS 2000):

$$[M][\ddot{u}] + [C][\dot{u}] + [K][u] = \{F\} \tag{35}$$

where $[M]$ and $[K]$ are the mass matrix and the stiffness matrix, respectively, and are given as

$$[M] = \sum_{i=1}^{NE} [M_i^e] \qquad \text{and} \qquad [K] = \sum_{i=1}^{NE} [K_i^e]. \tag{36}$$

$[M_i^e]$ is the individual element mass matrix, NE the number of elements and $[K_i^e]$ is the individual element stiffness matrix. $\{F\}$ is the applied harmonic force matrix and $[C]$ is the structural damping matrix. In practice, the damping matrix is difficult to determine, since in structural mechanics one is more interested in dry friction and hysteretic damping rather than viscous damping. Hence, the structural damping matrix $[C]$ is approximated as Rayleigh damping, as

$$[C] = \alpha_d[M] + \beta[K] \tag{37}$$

where α_d and β are the mass damping factor and stiffness damping factor, respectively. In most of the cases, the mass damping factor, α_d, is ignored (ANSYS 2000). Hence, the stiffness damping factors β can be written as

$$\beta = \sum_{j=1}^{NMAT} \beta_j[K_j] \tag{38}$$

where $[K_j]$ is the portion of the stiffness matrix based on material j, and $NMAT$ is the number of materials (layers) in the model. In this model, two materials and three layers (top, middle and bottom) were used, where the top and bottom were aluminium layers and the middle layer was an epoxy layer.

The damping matrix $[C]$ can also be expressed as follows:

$$[C] = \left(\frac{\eta}{\omega}\right)[K] \tag{39}$$

where η is the mechanical loss factor of the material. Hence, the damping factor β can also be expressed as

$$\beta = \frac{\eta}{\omega} = \frac{\eta}{2\pi f}, \qquad \text{more specifically, } \beta_M = \frac{\eta_M}{2\pi f} \tag{40}$$

where the subscript M denotes the material type. The values of the damping factors for aluminium and epoxy used in this model are listed in table 2.

In order to determine the ASI at a particular frequency, an arbitrary harmonic force is applied on three edges of the patch boundary. Using FEM, dynamic harmonic analysis is performed and the complex displacement responses at the points of force application are obtained for a frequency range of 120 kHz. Using the linear sums of interpolation functions of all elements, the required displacements are then obtained. Boundary conditions, both natural and essential, are included in the load vectors and stiffness matrix (Bathe 1996). Equation (35) was solved by the solution tool of ANSYS 5.6. The approach employed to determine ASI is described below. The harmonic load applied on the structure can be expressed as

$$\{F\} = \{F_R + F_I j\}e^{j\omega t} \tag{41}$$

where F_R and F_I are the real and imaginary components, respectively, of the applied harmonic force vector $\{F\}$. The resultant harmonic displacement is expressed as

$$[u] = [u_R + u_I j]e^{j\omega t} \tag{42}$$

where $[u]$ is the complex displacement vector and u_R and u_I are the real and imaginary components, respectively, of the displacement vector. The displacement is a complex term, due to the phase lag caused by the impedance of the system.

Substituting equations (41) and (42) into (35), the following equation is obtained:

$$\{[K] + j\omega[C] - \omega^2[M]\}[u_R + ju_I] = [F_R + jF_I]. \tag{43}$$

In matrix form, the above equation can be written as

$$\begin{bmatrix} -\omega^2[M] + [K] & -\omega[C] \\ \omega[C] & -\omega^2[M] + [K] \end{bmatrix} \begin{bmatrix} u_R \\ u_I \end{bmatrix} = \begin{bmatrix} F_R \\ F_I \end{bmatrix}. \tag{44}$$

The unknown displacements at each load point were obtained from the above equation. Using $\dot{u}_1 = j\omega u_1$, $\dot{u}_3 = j\omega u_3$, (figure 2), the ASI of the structure is given as

$$Z_s = \frac{F_{HE}}{\frac{j\omega}{m}\sum_1^m (u_{mR} + u_{mI})} + \frac{F_{BE}}{\frac{j\omega}{n\alpha_P}\sum_1^n (u_{nR} + u_{nI})} + \frac{F_{TE}}{\frac{j\omega}{n\alpha_P}\sum_1^n (u_{nR} + u_{nI})} \tag{45}$$

where the subscripts to force F, namely HE, BE and TE, indicate the horizontal, bottom and top sides, respectively, of the PZT patch. In this model n and m are 5 and 3, respectively.

The procedure used is the full solution method (FSM). Researchers like Bhalla and Soh (2004a) also used the FSM to prove the effectiveness of their impedance method. This is more accurate than the reduced solution method (RSM) used by Makkonen *et al* (2001).

3.4. Convergence test

In order for the FE analysis (ANSYS 2000) to produce accurate results, it is important to use an appropriate mesh size. Suitably fine meshing to realistically simulate the transfer of the PZT forces (Liang *et al* 1994) is necessary. Thus in the present research, for the two test specimens used, different sets of mesh sizes were employed until the model frequencies converged. Table 5 lists the details of mesh size employed for specimens 1 and 2. The model frequencies for set 2 and set 3 as given in table 5 are found to be in close proximity, thus indicating the convergence of the frequencies. Hence, set 3 was finally

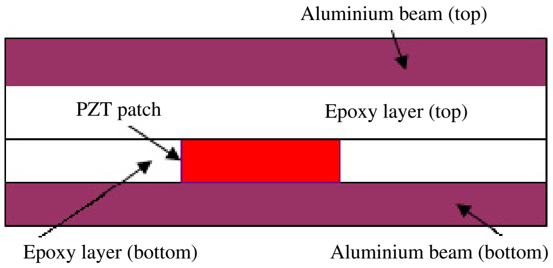

Figure 8. Layers used for meshing.

Table 5. Mesh sizes used for specimens 1 and 2.

Specimen no.	Set no.	Mesh size (m × m) ($10^{-3} \times 10^{-3}$)	Layer description
1	1	2 × 2	Aluminium beam (top)
		2 × 0.8	Epoxy layer (top)
		2 × 0.1	Epoxy layer (bottom)
		2 × 2	Aluminium beam (bottom)
	2	1.25 × 1	Aluminium beam (top)
		1.25 × 0.8	Epoxy layer (top)
		1.25 × 0.1	Epoxy layer (bottom)
		1.25 × 1	Aluminium beam (bottom)
	3	1 × 1	Aluminium beam (top)
		1 × 0.8	Epoxy layer (top)
		1 × 0.1	Epoxy layer (bottom)
		1 × 1	Aluminium beam (bottom)
2	1	1 × 1	Aluminium beam (top)
		1 × 0.9	Epoxy layer (top)
		1 × 0.15	Epoxy layer (bottom)
		1 × 1	Aluminium beam (bottom)

chosen for specimen 1. A similar procedure was adopted to select the mesh size for specimen 2 (table 5). Figure 8 shows the layers used for meshing the top and bottom aluminium layers and the two sandwiching epoxy layers. Table 6 lists the modal frequencies of the mesh size employed for specimen 1 with a description of the mode shape.

In order to ensure adequacy of the meshing, modal analysis was also performed. The element size should be sufficiently small (typically three to five nodal points per half-wavelength) to ensure an accurate solution (Makkonen *et al* 2001, Bhalla and Soh 2004a). All the modes of vibration in the frequency range of interest were analysed, from which the wavelengths of the excited modes were found

Table 6. Modal frequencies for different mesh sizes of specimen 1.

Mode	Modal frequency (kHz) Set 1	Set 2	Set 3	Mode shape description
1	0.330	0.327	0.327	Flexure
2	1.981	1.955	1.954	Flexure
3	5.183	5.104	5.099	Flexure
4	9.342	9.182	9.172	Flexure
5	10.457	10.457	10.456	Axial
6	14.167	13.903	13.883	Flexure
7	19.483	19.090	19.057	Flexure
8	25.226	24.674	24.621	Flexure
9	31.360	30.634	30.554	Flexure
10	31.391	31.362	31.361	Axial + Flexure
11	37.975	36.977	36.858	Flexure
12	45.017	43.712	43.542	Flexure
13	52.251	50.848	50.612	Flexure
14	52.537	52.239	52.233	Axial + Flexure
15	60.542	58.393	58.073	Flexure
16	69.045	66.343	65.918	Flexure
17	73.092	73.052	73.033	Axial + Flexure
18	78.029	74.682	74.132	Flexure
19	87.360	83.341	82.649	Flexure
20	93.797	91.721	91.041	Flexure
21	94.061	93.735	93.697	Axial + Flexure
22	97.379	94.638	94.407	Flexure
23	100.066	98.529	98.294	Flexure
24	107.356	102.909	102.021	Flexure
25	109.756	107.687	107.466	Flexure
26	114.179	112.753	111.629	Flexure
27	119.084	114.138	114.030	Axial + Flexure
28	120.957	119.452	118.982	Flexure

to be quite large compared with the element size considered. Figure 9 shows mode 28 and mode 18 (the highest excited mode), characterized by a natural frequency of 118.982 and 119.009 kHz for specimens 1 and 2, respectively. Hence, the criterion of sufficiently small element size is also clearly satisfied.

4. Experimental results and discussion

Using the ASI for the actuator and structure, obtained by FE analysis as described in the preceding sections, the value for A_0 is obtained from equation (24), which is then substituted into equation (28) to finally derive the admittance.

The experimental and analytical conductance and susceptance signatures of specimens 1 and 2 are shown in figures 10

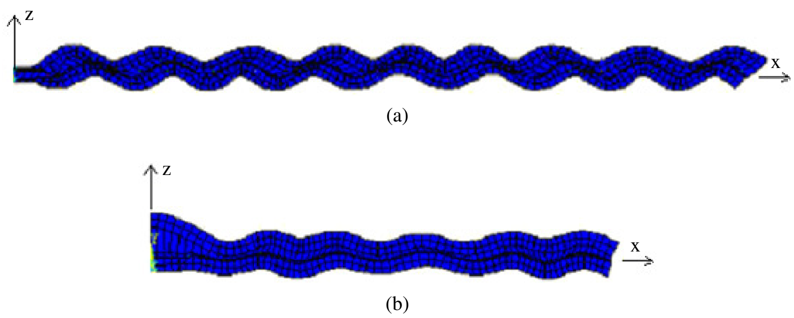

Figure 9. Graphical representation of the highest modal frequency of specimens 1 and 2. (a) Mode 28 (f = 118.982 kHz) for specimen 1. (b) Mode 18 (f = 119.099 kHz) for specimen 2.

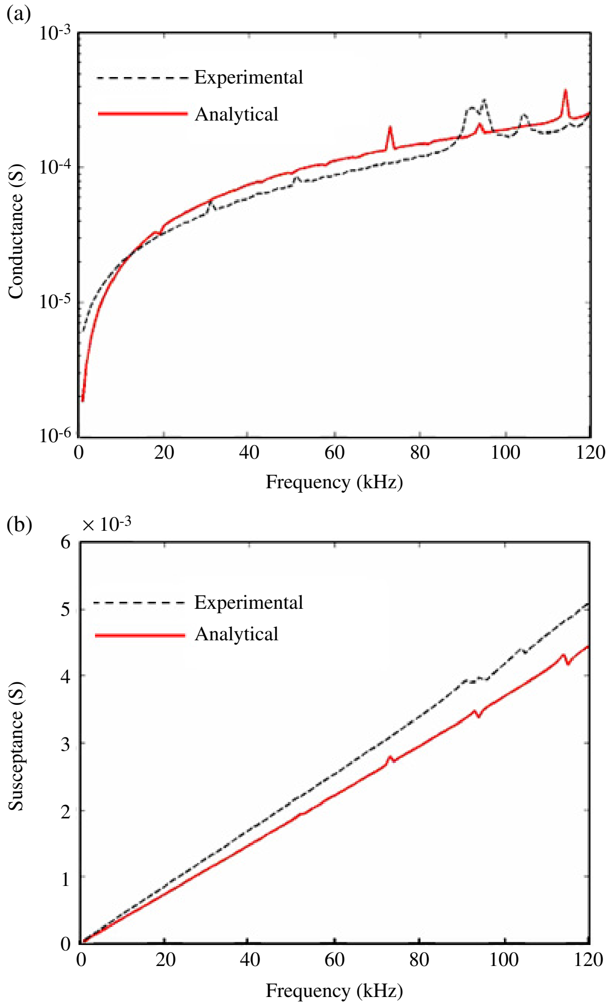

Figure 10. Experimental and analytical signatures of specimen 1: (a) conductance and (b) susceptance.

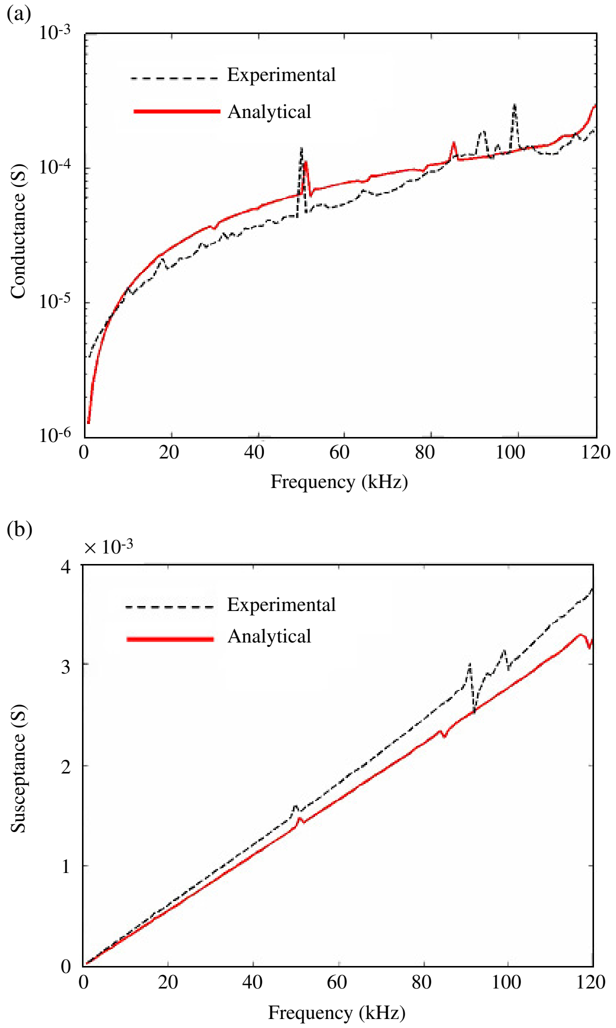

Figure 11. Experimental and analytical signatures of specimen 2: (a) conductance and (b) susceptance.

and 11. In the considered range of frequency ($<$120 kHz), both experimental and analytical peaks were observed. The peaks in signatures are dependent on the type of material of the test specimen.

The peak matches of conductance signatures at 95 kHz for specimen 1 and 50 kHz for specimen 2 are clearly evident. Difficulty in using epoxy to bond the aluminium layers could be one of the reasons for the variations of other peaks, but generally the trends are the same.

5. Conclusions

In this paper, a new ASI concept is introduced where the ASI-based admittance formulations considered both the vibrations in the length and thickness directions (extensional and longitudinal actuations) of the PZT patch. Thus the formulations are generic and impose no constraints like the thickness limitation of the PZT patch, and can be used for all PZT patches. Vibration of the thickness dimension (longitudinal actuation) of the PZT patch, which was previously neglected by other researchers, was successfully employed in our formulations and the confined behaviour of the PZT patch was demonstrated. To validate our model, two sandwiched beam specimens fabricated using aluminium beams sandwiching an epoxy layer were used. The ASI-based analytical admittance signatures were compared with the experimental signatures, and the trends were found to be in good agreement.

Acknowledgments

The authors would like to acknowledge Mr Suresh Bhalla and Mrs Rupali Suresh for their kind support in both the technical aspects and the mathematical formulations.

References

Agilent Technologies, USA 2004 *Test and Measurement Catalogue*

ANSYS Inc., Canonsburg, PA, USA 2000 *ANSYS Reference Manual: Release 5.6*

Ayres J W, Lalande F, Chaudhry Z and Rogers C A 1998 Qualitative impedance based health monitoring of civil infrastructures *Smart Mater. Struct.* **7** 599–605

Bathe K J 1996 *Finite Element Procedures* (Upper Saddle river, NJ: Prentice-Hall) p 07458

Bhalla S and Soh C K 2004a Structural health monitoring by piezo-impedance transducers I: modeling *J. Aerosp. Eng. ASCE* **17** 154–65

Bhalla S and Soh C K 2004b Structural impedance based damage diagnosis by piezo-transducers *Earthq. Eng. Struct. Dyn.* **32** 1897–1916

Doebling S W, Farrar C R and Prime M B 1998 A summary review of vibration-based damage identification methods *The Shock Vib. Digest* **30** 91–105

Giurgiutiu V, Reynolds A and Rogers C A 1999 Experimental investigation of electromechanical impedance health monitoring for spot-welded structural joints *J. Intell. Mater. Syst. Struct.* **10** 802–12 (ed N M Wereley)

Giurgiutiu V and Zagrai A N 2000 Characterization of piezoelectric wafer active sensors *J. Intell. Mater. Syst. Struct.* **11** 959–76

Hewlett Packard 1996 HP LF 4192A impedance analyzer *Operation Manual* Japan

Liang C, Sun F P and Rogers C A 1994 Coupled electro-mechanical analysis of adaptive material systems—determination of the actuator power consumption and system energy transfer *J. Intell. Mater. Syst. Struct.* **5** 12–20

Makkonen T, Holappa A, Ella J and Salomaa M M 2001 Finite element simulations of thin-film composite BAW resonators *IEEE Trans. Ultrason. Ferroelectr. Freq. Control* **48** 1241–58

Naidu A S K and Soh C K 2004 Identifying damage location with admittance signatures of smart piezo-transducers *J. Intell. Mater. Syst. Struct.* **15** 627–42

Park G, Cudney H H and Inman D J 2000 Impedance-based health monitoring of civil structural components *J. Infrastruct. Syst. ASCE* **6** 153–60

Park G, Cudney H H and Inman D J 2001 Feasibility of using impedance-based damage assessment for pipeline structures *Earthq. Eng. Struct. Dyn.* **30** 1463–74

Park G, Sohn H, Farrar C R and Inman D J 2003 Overview of piezoelectric impedance-based health monitoring and path forward *The Shock Vib. Digest, SAGE Publications* **35** 451–63

Peairs D M, Park G and Inman D J 2004 Improving accessibility of the impedance-based structural health monitoring method *J. Intell. Mater. Syst. Struct.* **15** 129–39

PI Ceramic 2004 *Product Information Catalogue* Lindenstrabe, Germany http://www.piceramic.de

Raja S, Sreedeep R and Prathap G 2004 Bending behavior of hybrid-piezoelectric sandwich beams *J. Intell. Mater. Syst. Struct.* **15** 611–9

RS Components 2004 *Product Information Catalogue* Northants, UK http://www.rs-components.com

Sensor Technology Limited 1995 *Product Information Catalogue* Collingwood

Soh C K, Tseng K K H, Bhalla S and Gupta A 2000 Performance of smart piezoceramic patches in health monitoring of a RC bridge *Smart Mater. Struct.* **9** 533–42

Sun F P, Chaudry Z, Rogers C A, Majmundar M and Liang C 1995 Automated real-time structure health monitoring via signature pattern recognition *Proc. Smart Structures Materials Conf. (San Diego, CA, Feb. 27–March 1)*; *Proc. SPIE* **2443** 236–47

Wang X and Shen Y 1998 On the characterization of piezoelectric actuators attached to structures *Smart Mater. Struct.* **7** 389–95

Wetherhold R, Messer M and Patra A 2003 Optimization of directionally attached piezoelectric actuators *J. Eng. Mater. Technol.* **125** 148–52

Zhou S W, Liang C and Rogers C A 1996 An impedance-based system modeling approach for induced strain actuator-driven structures *J. Vib. Acoust. ASME* **118** 323–31